

Gate-Controlled Transmission of Quantum Hall Edge States in Bilayer Graphene

Jing Li,¹ Hua Wen,¹ Kenji Watanabe,² Takashi Taniguchi,² and Jun Zhu^{1,3,*}

¹*Department of Physics, The Pennsylvania State University, University Park, Pennsylvania 16802, USA*

²*National Institute for Material Science, 1-1 Namiki, Tsukuba 305-0044, Japan*

³*Center for 2-Dimensional and Layered Materials, The Pennsylvania State University, University Park, Pennsylvania 16802, USA*

 (Received 11 September 2017; revised manuscript received 1 December 2017; published 31 January 2018)

The edge states of the quantum Hall and fractional quantum Hall effect of a two-dimensional electron gas carry key information of the bulk excitations. Here we demonstrate gate-controlled transmission of edge states in bilayer graphene through a potential barrier with tunable height. The backscattering rate is continuously varied from 0 to close to 1, with fractional quantized values corresponding to the sequential complete backscattering of individual modes. Our experiments demonstrate the feasibility to controllably manipulate edge states in bilayer graphene, thus opening the door to more complex experiments.

DOI: [10.1103/PhysRevLett.120.057701](https://doi.org/10.1103/PhysRevLett.120.057701)

The edge states of quantum Hall (QH) and fractional quantum Hall (FQH) effects are not only fascinating one-dimensional quantum fluid with rich dynamics of their own [1] but also provide access to the unconventional charge and statistics of the quasiparticle excitations of the bulk many-body ground states [2–4]. A well-known example is the even-denominator FQH state at filling factor $\nu = 5/2$ in GaAs quantum wells [5,6], where a ground state with non-Abelian excitations has long been hypothesized [7], yet experimental confirmation remains difficult and controversial [8–10]. The $5/2$ state in GaAs is fragile and the electrostatic environment of high-quality GaAs samples is quite complex [11]. Recent technological advances have enabled remarkable strides in the quality of the two-dimensional electron gas (2DEG) in graphene [12,13]. Bilayer graphene, for example, exhibits a plethora of broken-symmetry QH, FQH, and QH ferromagnetic states [14–19]. Importantly, even-denominator FQH states with large gaps of a few kelvin have been observed [20–22]. The thin profile of a graphene device enables smaller and more precise nanostructures, such as demonstrated in our previous work on the quantum valley Hall kink states and valleytronic operations in bilayer graphene [23,24]. The simultaneous advances of sample quality and device fabrication techniques now enable more sophisticated edge state experiments in graphene. Past experiments have shown that naturally formed, smooth potential interfaces in a p - n [25–28] or p - n - p or p - p' - p junction [29–33] allow edge states to fully equilibrate. Spin polarization imposes a selection rule at low Landau levels [31,32]. Klimov *et al.* observed partial equilibration at a p - n junction where a barrier is present although the barrier height is not tunable [34]. Recently, Zimmermann *et al.* created a quantum point contact (QPC) geometry in graphene using a pair of top split gates and showed its control over the transmission of the edge modes [32]. This control, however, is less

straightforward since carriers underneath the split gates cannot be depleted and produce edge states of their own that assist in tunneling. A clean QPC action, where a gate-tuned potential barrier controls the interaction between two quantum Hall edges, has not been realized in graphene.

In this Letter, we report on gate-controlled transmission of edge states between two lateral QH states in bilayer graphene. We use a dual split-gated structure to control the filling factor of the left and right QH states independently and a fifth gate to modulate the height of the tunnel barrier between the two. The tunneling resistance varies with the barrier height and exhibits plateaus that correspond to complete backscattering of individual edge states one by one. The experimental observations are quantitatively captured by finite element simulations of the device. This study is a proof-of-concept demonstration towards the construction of more sophisticated structures, such as a Fabry-Perot interferometer.

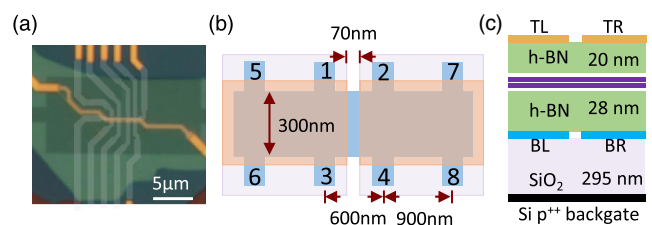


FIG. 1. (a) An optical micrograph of device 47. The bottom split gates are made of multilayer graphene (dark squares). The top split gates are Au. The bilayer graphene is etched into a multiprobe Hall bar highlighted in white. The top and bottom h-BN sheets appear in green and dark blue shades, respectively. (b), (c) Schematics of the top and side views of device 47. Orange and light purple shades illustrate the top and bottom split gates, respectively. The parameters of device 47 are given in the diagrams.

Figure 1(a) shows an optical micrograph of one of our devices (device 47) with its top and side views schematically shown in Figs. 1(b) and 1(c) respectively. The split junction is 70 nm in width and 300 nm in length in both devices 43 and 47. The devices are similar in structure and fabrication to those used to demonstrate the quantum valley Hall kink states [23]. In device 47, the gating efficiencies are, respectively, 8.04 and $6.00 \times 10^{11} \text{ cm}^{-2} \text{ V}^{-1}$ for the top (TL and TR) and bottom (BL and BR) split gates. They correspond to thicknesses of 20 and 28 nm, respectively, for the top and bottom hexagonal-Boron Nitride (h-BN) dielectric layers, with $\epsilon = 3.0$ [23].

Landau levels (LLs) form when a perpendicular magnetic field is applied [17,19]. Using the four split gates, we can vary the filling factors ν_L and ν_R , and the displacement electric fields D_L and D_R of the left and right QH states independently. We pass a constant current through the entire device and measure R_{xx} and R_{xy} of each side, as well as R_{xx} across the junction simultaneously using standard low-frequency lock-in techniques. Early onset of the symmetry-broken integer QH states and the appearance of FQH states attest to the reasonably high quality of our devices (see Fig. S1 in Supplemental Material (SM) [35]). Data presented here are acquired at $B = 18 \text{ T}$ and $T = 0.3 \text{ K}$. Figure 2(a) plots examples of R_{xy}^{-1} and R_{xx} obtained on device 47. Both sides exhibit well-resolved integer QH states in the p -type carrier regime. Using these

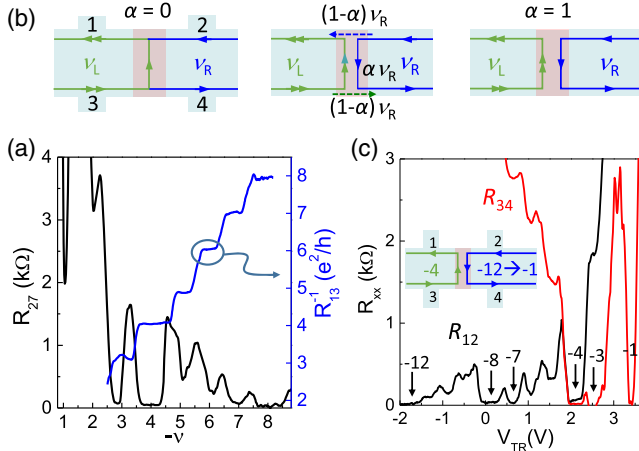


FIG. 2. (a) R_{27} (black curve, left axis) and R_{13}^{-1} (blue curve, right axis) vs filling factor ν measured on the right and left side of device 47, respectively. $R_{27}(\nu_R)$ is measured by sweeping V_{TR} while fixing $V_{TL} = 0 \text{ V}$. $R_{13}(\nu_L)$ is measured by sweeping V_{TL} while fixing $V_{TR} = 0 \text{ V}$. In both measurements, $V_{BL} = V_{BR} = -4.5 \text{ V}$ and $V_{Si} = -20 \text{ V}$. From device 47. (b) The edge states flow diagram in a unipolar junction with $|\nu_L| > |\nu_R|$. The left, middle, and right panels show perfect transmission, partial backscattering, and complete backscattering of the right side edge states, respectively. (c) R_{12} (black trace) and R_{34} (red trace) as a function of V_{TR} . $V_{BR} = -5.0 \text{ V}$. ν_R varies from -12 to -1 as the inset shows. $V_{Si} = -30 \text{ V}$. Arrows indicate the integer fillings of ν_R . $\nu_L = -4$ is fixed by setting $V_{BL} = -4.02 \text{ V}$, $V_{TL} = 1.4 \text{ V}$. From device 43.

measurements, we select well-developed QH regimes for subsequent edge tunneling measurements. Results reported here focus on unipolar p - p junctions.

When both sides of the junction are positioned at integer filling factors as illustrated in Fig. 2(b), edge states propagate at the sample boundary and interact along the line junction, the potential of which is controlled by V_{Si} applied to the doped silicon backgate in Fig. 1(c). Here we have set $|\nu_L| > |\nu_R|$. The junction may backscatter a fraction of the edge states from the right, as the middle panel of Fig. 2(b) shows. The backscattering rate α is controlled by the height of the junction potential. $\alpha = 0$ in the left-hand panel corresponds to the situation of perfect transmission while $\alpha = 1$ in the right-hand panel depicts the situation of complete backscattering.

Using the Landauer-Büttiker formula for edge state transport, we can relate α to R_{xx} measured across the junction, e.g., R_{12} or R_{34} in Fig. 2(c), and obtain

$$R_{34} = \frac{\alpha}{1 - \alpha\nu_R} \frac{1}{e^2} h, \quad (1)$$

which is along the bottom side of the sample where the edge states flow from left to right (assuming $|\nu_L| > |\nu_R|$). Similarly, along the top side of the sample, we find

$$R_{12} = \left(\frac{1}{1 - \alpha\nu_R} - \frac{1}{\nu_L} \right) \frac{h}{e^2}. \quad (2)$$

The expressions of R_{12} or R_{34} exchange with one another in the case of $|\nu_L| < |\nu_R|$ or when the direction of the magnetic field is reversed.

Equations (1) and (2) enable us to measure the edge state backscattering rate α directly, similar to past studies in GaAs [36–38]. R_{34} vanishes in the case of $\alpha = 0$, where a $|\nu_R|$ number of edge states flow through the junction along both top and bottom sides of the sample without backscattering. A finite R_{34} , together with simultaneously vanishing R_{xx} of the bulk QH states, indicates backscattering at the junction.

An example of a transparent junction is given in Fig. 2(c) using data in device 43. Here, we set $\nu_L = -4$ and sweep gate voltage V_{TR} to change ν_R from -12 to -1 . V_{Si} is fixed at -30 V . Both R_{12} (black line) and R_{34} (red line) vs V_{TR} are plotted. From $-4 \leq \nu_R < -1$, Eq. (1) describes R_{34} , whereas from $-12 < \nu_R \leq -4$, Eq. (1) describes R_{12} instead. We see immediately that $\alpha = 0$ when ν_R is at the integer fillings of $-1, -3, -4, -7, -8$, and -12 ; i.e., the junction is transparent. In fact, nonzero R_{12} (or R_{34}) observed at other integer fillings of ν_R ($\nu_R = -2, -5, -6$, and so on) is likely due to contributions from nonzero R_{xx} of the bulk, as R_{27} shown in Fig. 2(a) suggests. As we will show in the simulations, $V_{Si} = -30 \text{ V}$ corresponds to a p - p' junction with a smooth interface potential profile, similar to what is studied in Refs. [25–28].

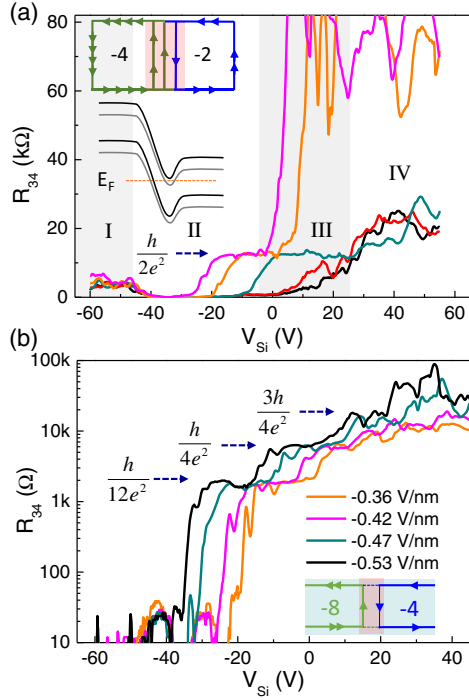


FIG. 3. (a) R_{34} as a function of V_{Si} . From left (magenta) to right (black): $D_R = -0.35, -0.30, -0.20, -0.10,$ and -0.05 V/nm. $D_L = -0.2$ V/nm for all traces. $(\nu_L, \nu_R) = (-4, -2)$. Positive D corresponds to an electric field pointing up. See Ref. [23] for the definition of D and how we control ν and D independently. Transmission regimes I–IV are marked for the $D_R = -0.20$ V/nm trace (dark cyan). The dashed arrow indicates resistance value of $h/2e^2 = 12.9$ k Ω . Insets illustrate the flow of the edge states and the potential profile across the junction in regime III. (b) R_{34} vs V_{Si} in the case of $(\nu_L, \nu_R) = (-8, -4)$ as the inset illustrates. $D_L = -0.21$ V/nm; D_R varies as labeled in the plot. Dashed arrows mark resistance values of $h/12e^2, h/4e^2,$ and $3h/4e^2$. From device 47.

Next, we investigate the effect of the junction potential on α . In Fig. 3(a), we plot R_{34} as a function of V_{Si} , while fixing both filling factors ν_L and ν_R to be $(\nu_L, \nu_R) = (-4, -2)$. Here, $D_L = -0.2$ V/nm is fixed on the left while different traces correspond to different values of D_R . The D field controls the energies of the bilayer graphene LL spectrum [19]. A large D field promotes the splitting at $\nu = \pm 1$ and ± 3 . A quantitative LL diagram between $-4 < \nu < +4$ is given in Fig. S2 of the Supplemental Material [35]. In Fig. 3(a), we label the four distinct regimes for the dark cyan trace corresponding to $D_R = -0.2$ V/nm. In regime II, R_{34} is close to zero, which indicates the perfect transmission of both edge modes of ν_R across the junction. As V_{Si} increases further, R_{34} becomes finite and eventually reaches large values (regimes III and IV). This behavior corresponds to the increase of the potential barrier between the two QH states as p -type carriers in the junction are increasingly depleted, eventually causing all edge states to backscatter completely. To the left of regime II, a moderate increase of R_{34} is also observed

when V_{Si} becomes very negative and the junction becomes heavily p doped. This is labeled as regime I in the plot. Finite bulk conduction across the junction is likely responsible.

What is most striking in Fig. 3(a) is the appearance of a wide plateau in R_{34} (regime III in the plot). The resistance value of the plateau is close to $h/2e^2$, which corresponds to $\alpha = 1/2$ in Eq. (1). The appearance of the quantization is intuitive when considering the evolution of the bulk LLs inside the junction. As the insets of Fig. 3(a) show, when E_F resides between the first and second LLs inside the junction, one edge mode is completely backscattered while the other fully transmits through the junction. As our data in Fig. 3(a) shows, the $h/2e^2$ plateau appears only when $|D_R| > \sim 0.15$ V/nm. This is consistent with our prior findings on the D -field dependence of the LLs in bilayer graphene [19].

Resistance plateaus in R_{34} appear in several other combinations of ν_L and ν_R and are consistent with the above selective complete backscattering interpretation. Figure 3(b) shows another example at $(\nu_L, \nu_R) = (-8, -4)$. A few more scenarios are given in the SM [35]. Although the quantization in Fig. 3(b) is not as well developed as that shown in Fig. 3(a), R_{34} exhibits clear plateaus or shoulders close to $h/12e^2, h/4e^2,$ and $3h/4e^2$ expected for $\alpha = 1/4, 1/2,$ and $3/4$, respectively. These plateaus suggest the sequential complete backscattering of 1, 2, and 3 modes before all edge states are backscattered. As V_{Si} is swept from -60 to $+50$ V, the 4 orders of magnitude change of R_{34} corresponds to a change of α from 0 to roughly 0.9. This large tunability of α attests to the effective control of V_{Si} on the junction potential in our devices.

It is interesting to note that in both Figs. 3(a) and 3(b) the onsets of regimes III and IV exhibit a systematic shift towards negative V_{Si} 's as D_R becomes more negative, i.e., a positive $\Delta V_{Si}/\Delta D_R$. In Fig. 4(a), we plot the magnitude of $\Delta V_{Si}/\Delta D_R$ at several (ν_L, ν_R) scenarios as labeled in the plot. Meanwhile, the onset of regime II appears insensitive to D_R . These behaviors cannot be explained by the change of the bulk LLs with D_R . Instead, we look to practical considerations such as the impact of misalignment between the top and bottom split gates. Using a finite element simulation tool (COMSOL, multiphysics package), we simulated the gating effect of all five gates in device 47. The results are summarized in Fig. 4 while the methods and more details are given in the SM [35]. The carrier density profile $n(x)$ across the split junction is computed and converted to a filling factor profile $\nu(x)$. Figure 4(b) plots $\nu(x)$ at selected V_{Si} 's from -50 to 30 V for two slightly different structures. The dashed lines correspond to the perfectly aligned gates shown in the upper inset of the graph. The solid lines correspond to the scenario shown in the lower inset, where the TR gate shifts into the junction by $d = 15$ nm. The overall shape of $\nu(x)$ and its evolution with V_{Si} are what is expected intuitively. The $V_{Si} = 10$ V

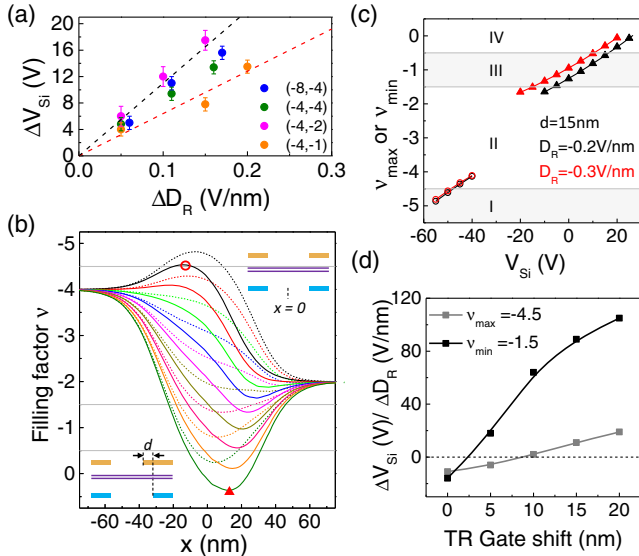


FIG. 4. (a) Measured ΔV_{Si} vs ΔD_R in different cases of (ν_L, ν_R) as labeled in the plot. The slope of the red dashed line corresponds to the value of $\Delta V_{Si}/\Delta D_R$ at $d = 10$ nm on the black curve in (d). The slope of the black dashed line corresponds to $d = 20$ nm. (b) Simulated filling factor profile $\nu(x)$ across the junction at selected values of V_{Si} from -50 V (black) to 30 V (olive) in 10 V steps. $(\nu_L, \nu_R) = (-4, -2)$, $D_L = -0.2$ V/nm, and $D_R = -0.3$ V/nm. The junction center $x = 0$ is marked in the upper inset. The dashed curves correspond to perfect gate alignment, as illustrated in the upper inset. The solid curves correspond to a TR gate shift of 15 nm into the junction, as illustrated in the lower inset. Other dimension parameters used that of device 47. (c) ν_{max} vs V_{Si} (open circles) and ν_{min} vs V_{Si} (solid triangles) obtained from simulating the gate arrangement shown in the lower inset of (b) with $d = 15$ nm and $D_R = -0.2$ (black symbols) and -0.3 V/nm (red symbols). $D_L = -0.2$ V/nm is fixed for both scenarios. The onset of regimes II–IV corresponds to $V_{Si} = -47.7$, -6.2 , and 16.6 V, respectively, for $D_R = -0.2$ V/nm and $V_{Si} = -48.7$, -15.1 , and 10.5 V, respectively, for $D_R = -0.3$ V/nm. (d) Simulated $\Delta V_{Si}/\Delta D_R$ vs the TR gate shift distance d for $\nu_{max} = -4.5$ and $\nu_{min} = -1.5$, as labeled in the plot.

curve, for example, resembles the diagram shown in the inset of Fig. 3(a). The comparison of the $d = 0$ and 15 nm cases shows that the shift of the TR gate has a large effect on the minima of $\nu(x)$, ν_{min} , which shift towards the right side but much smaller effect on the maxima of $\nu(x)$, ν_{max} . We shall see that it correctly captures the behavior of $\Delta V_{Si}/\Delta D_R$ in different regimes.

To connect with experiment, in Fig. 4(c), we plot ν_{max} (open circles) and ν_{min} (solid triangles) obtained from the $d = 15$ nm curves in Fig. 4(b). Two sets of V_{TR} 's and V_{BR} 's corresponding to $D_R = -0.2$ and -0.3 V/nm, respectively, are used in the simulations and the results are plotted in black and red symbols, respectively, in Fig. 4(c). Using the diagram shown in the inset of Fig. 3(a), we associate the onsets of regimes III and IV with $\nu_{min} = -1.5$ and -0.5 , respectively, and similarly

associate the onset of regime II with $\nu_{max} = -4.5$. This allows us to identify and label the four transmission regimes in Fig. 4(c). Their onset voltages in V_{Si} agree with measurements in Fig. 3(a) very well for both D_R values simulated. Indeed, a positive $\Delta V_{Si}/\Delta D_R$ is observed for the onsets of regimes III and IV while the onset of regime II remains nearly stationary. In the SM, we analyze the contribution of individual gates to provide a physical picture for the results of the simulations.

Simulations and analysis similar to that shown in Figs. 4(b) and 4(c) are carried out for $d = 0, 5, 10, 15,$ and 20 nm, and the $\Delta V_{Si}/\Delta D_R$ obtained at $\nu_{max} = -4.5$ and $\nu_{min} = -1.5$ are plotted in Fig. 4(d). Here, $\Delta V_{Si}/\Delta D_R$ is calculated by linearly interpolating results at $D_R = -0.2$ and -0.3 V/nm. $\Delta V_{Si}/\Delta D_R$ is negligible for the onset of regime II at any d values while $\Delta V_{Si}/\Delta D_R$ increases with increasing d for the onset of regime III, as expected. Using the simulated $\Delta V_{Si}/\Delta D_R$ as the slope, we plot two dashed lines in Fig. 4(a). The black dashed line corresponds to $d = 20$ nm while the red dashed line corresponds to $d = 10$ nm. The majority of our data fall within the area in between. A misalignment of this magnitude is consistent with the precisions of our fabrication methods [23]. We are puzzled by the spread of the data as all of them are acquired on device 47. We note that our simple electrostatics model does not take into account the specifics of the LL structure, the shape of the density of states, and the self-screening of the bilayer graphene, which may all play a role in determining the precise values of the onsets. Overall, the success of the simulation highlights an important advantage of graphene gating structures, i.e., their relatively simple and deterministic electrostatic environment. This advantage can be used to facilitate simulation-guided design of future experiments and foster a stronger connection between theory and experiment.

To summarize, we demonstrate potential-controlled transmission of quantum Hall edge states in bilayer graphene by employing independent gate controls on relevant parameters of the system. The backscattering rate is continuously tunable over a large range and sequential complete backscattering of individual edge modes is observed and well understood in numerical simulations using experimental device parameters. Our results are encouraging first steps towards building more complex nanostructures, such as an electron interferometer, to probe the charge and statistics of quasiparticles in the QH and FQH regimes of bilayer graphene.

We thank Fan Zhang and Allan H. MacDonald for helpful discussions. Work at Penn State is supported by the NSF through NSF-DMR-1506212. Work at NIMS is supported by the Elemental Strategy Initiative conducted by the MEXT, Japan and JSPS KAKENHI Grant No. JP15K21722. Part of this work was performed at the NHMFL, which was supported by the NSF through

NSF-DMR-1157490 and the State of Florida. We thank Jan Jaroszynski of the NHMFL for experimental assistance.

*Corresponding author.

jzhu@phys.psu.edu

- [1] A. M. Chang, *Rev. Mod. Phys.* **75**, 1449 (2003).
- [2] V. J. Goldman and B. Su, *Science* **267**, 1010 (1995).
- [3] R. de-Picciotto, M. Reznikov, M. Heiblum, V. Umansky, G. Bunin, and D. Mahalu, *Nature (London)* **389**, 162 (1997).
- [4] A. Stern, *Ann. Phys. (Amsterdam)* **323**, 204 (2008).
- [5] R. L. Willett, *Rep. Prog. Phys.* **76**, 076501 (2013).
- [6] X. Lin, R. Du, and X. Xie, *Natl. Sci. Rev.* **1**, 564 (2014).
- [7] G. Moore and N. Read, *Nucl. Phys.* **B360**, 362 (1991).
- [8] R. L. Willett, L. N. Pfeiffer, and K. W. West, *Proc. Natl. Acad. Sci. U.S.A.* **106**, 8853 (2009).
- [9] I. P. Radu, J. B. Miller, C. M. Marcus, M. A. Kastner, L. N. Pfeiffer, and K. W. West, *Science* **320**, 899 (2008).
- [10] H. Fu, P. Wang, P. Shan, L. Xiong, L. N. Pfeiffer, K. West, M. A. Kastner, and X. Lin, *Proc. Natl. Acad. Sci. U.S.A.* **113**, 12386 (2016).
- [11] W. Pan, J. S. Xia, V. Shvarts, D. E. Adams, H. L. Stormer, D. C. Tsui, L. N. Pfeiffer, K. W. Baldwin, and K. W. West, *Phys. Rev. Lett.* **83**, 3530 (1999).
- [12] C. R. Dean *et al.*, *Nat. Nanotechnol.* **5**, 722 (2010).
- [13] L. Wang *et al.*, *Science* **342**, 614 (2013).
- [14] P. Maher, C. R. Dean, A. F. Young, T. Taniguchi, K. Watanabe, K. L. Shepard, J. Hone, and P. Kim, *Nat. Phys.* **9**, 154 (2013).
- [15] A. Kou, B. E. Feldman, A. J. Levin, B. I. Halperin, K. Watanabe, T. Taniguchi, and A. Yacoby, *Science* **345**, 55 (2014).
- [16] P. Maher *et al.*, *Science* **345**, 61 (2014).
- [17] B. M. Hunt *et al.*, *Nat. Commun.* **8**, 948 (2017).
- [18] A. V. Rozhkov, A. O. Sboychakov, A. L. Rakhmanov, and F. Nori, *Phys. Rep.* **648**, 1 (2016).
- [19] J. Li, Y. Tupikov, K. Watanabe, T. Taniguchi, and J. Zhu, *Phys. Rev. Lett.* **120**, 047701 (2018).
- [20] D. K. Ki, V. I. Fal'ko, D. A. Abanin, and A. F. Morpurgo, *Nano Lett.* **14**, 2135 (2014).
- [21] A. A. Zibrov, C. R. Kometter, T. Taniguchi, K. Watanabe, M. P. Zaletel, and A. F. Young, *Nature (London)* **549**, 360 (2017).
- [22] J. I. A. Li, C. Tan, S. Chen, Y. Zeng, T. Taniguchi, K. Watanabe, J. Hone, and C. R. Dean, *Science* **358**, 648 (2017).
- [23] J. Li, K. Wang, K. J. McFaul, Z. Zern, Y. Ren, K. Watanabe, T. Taniguchi, Z. Qiao, and J. Zhu, *Nat. Nanotechnol.* **11**, 1060 (2016).
- [24] J. Li, R.-X. Zhang, Z. Yin, J. Zhang, K. Watanabe, T. Taniguchi, C. Liu, and J. Zhu, [arXiv:1708.02311v1](https://arxiv.org/abs/1708.02311v1).
- [25] D. Abanin and L. Levitov, *Science* **317**, 641 (2007).
- [26] B. Huard, J. A. Sulpizio, N. Stander, K. Todd, B. Yang, and D. Goldhaber-Gordon, *Phys. Rev. Lett.* **98**, 236803 (2007).
- [27] J. R. Williams, L. Dicarlo, and C. M. Marcus, *Science* **317**, 638 (2007).
- [28] S. Matsuo, S. Takeshita, T. Tanaka, S. Nakaharai, K. Tsukagoshi, T. Moriyama, T. Ono, and K. Kobayashi, *Nat. Commun.* **6**, 8066 (2015).
- [29] B. Ozyilmaz, P. Jarillo-Herrero, D. Efetov, D. A. Abanin, L. S. Levitov, and P. Kim, *Phys. Rev. Lett.* **99**, 166804 (2007).
- [30] S.-G. Nam, D.-K. Ki, J. W. Park, Y. Kim, J. S. Kim, and H.-J. Lee, *Nanotechnology* **22**, 415203 (2011).
- [31] F. Amet, J. R. Williams, K. Watanabe, T. Taniguchi, and D. Goldhaber-Gordon, *Phys. Rev. Lett.* **112**, 196601 (2014).
- [32] K. Zimmermann, A. Jordan, F. Gay, K. Watanabe, T. Taniguchi, Z. Han, V. Bouchiat, H. Sellier, and B. Sacépé, *Nat. Commun.* **8**, 14983 (2017).
- [33] H. Overweg *et al.*, *Nano Lett.* **17**, 2852 (2017).
- [34] N. N. Klimov, S. T. Le, J. Yan, P. Agnihotri, E. Comfort, J. U. Lee, D. B. Newell, and C. A. Richter, *Phys. Rev. B* **92**, 241301 (2015).
- [35] See Supplemental Material at <http://link.aps.org/supplemental/10.1103/PhysRevLett.120.057701> for device characteristics, a Landau level diagram of bilayer graphene in a magnetic field, additional data on gate-controlled transmission of edge states, and a detailed description of the COMSOL simulations.
- [36] R. J. Haug, A. H. MacDonald, P. Streda, and K. von Klitzing, *Phys. Rev. Lett.* **61**, 2797 (1988).
- [37] S. Washburn, A. B. Fowler, H. Schmid, and D. Kern, *Phys. Rev. Lett.* **61**, 2801 (1988).
- [38] W. Kang, H. Stormer, L. Pfeiffer, K. Baldwin, and K. West, *Nature (London)* **403**, 59 (2000).